Electronic Supplementary Material (ESI) for Nanoscale.

Playing *catch and release* with single molecules: Mechanistic insights into plasmon-controlled nanogaps.

Katrin F. Domke*[a] and Albert C. Aragonès*[b]

[a] *University of Duisburg-Essen, Faculty of Chemistry, Universitätsstr. 5, 45141 Essen; Max Planck Institute for Polymer Research, Ackermannweg 10, 55128 Mainz, Germany. E-mail: katrin.domke@uni-due.de.* [b] *Departament de Ciència de Materials i Química Física, Universitat de Barcelona, Marti i Franquès 1, 08028, Barcelona, Spain & Institut de Química Teòrica i Computacional (IQTC), Universitat de Barcelona, Diagonal 645, 08028, Barcelona, Spain. E-mail: acortijos@ub.edu.*

Contents

1 Additional technical details

1.1 Plasmon-supported break-junction setup

Plasmon-supported break junction (PBJ) technique is explained elsewhere.[1] PBJ experiments were performed with an electrically and mechanically isolated custom-designed setup based on a commercial electrochemical scanning tunnelling microscope (EC-STM) (Keysight Technologies -former Agilent- 5420) coupled to a HeNe laser (632.8 nm; REO LSRP-3501, 35 mW maximum output power, linearly polarised) in a side-illumination configuration with an angle of 55°between the focusing/collection objective and the substrate surface normal.[2] An Olympus 50x long working-distance objective (WD = 10.6 mm, NA = 0.5) is used to focus the laser beam onto the interelectrode gap. Gray filters for laser beam power control, mirrors, pinholes, as well as other basic optical elements were purchased from Thorlabs. A metal-oxide semiconductor (CMOS) camera (EoSens MC 1362, Mikrotron) is placed in the beam path with a 50:50 beam splitter (Thorlabs CM1BS013) mounted onto a removable holder to visually examine the farfield focus and gap illumination. The current I(t) readout from the STM are captured using a NI-DAQmx/BNC-2110 (National Instruments analog-digital converter interface acquisition) system adjusted to a sampling rate of 10 KHz, analysed with a home-written Python codes, and plotted with Matplotlib.[3]

1.2 Single-molecule junction experiments

In the single-molecule experiments, the fixed interelectrode nanogap was established between the STM tip and the substrate, tuning the set-point (tunneling) current, to be in the order of the molecular size of 1,4-benzenedithiol (1 nm in accordance with the literature for a bridge contact geometry).[4,5] When the nanogap is stabilised and shows a constant I_t vs time, the I_t feedback is turned off. The current between tip and substrate STM electrodes is continuously monitored as I(t). A sudden current increase to the background current I_{DIS}, commonly referred to as a blink, appears when a target molecule is spontaneously connected to both electrodes in the nanogap, thus increasing the detected current (I_{CON}). The (spontaneous) collapse of the junction (i.e. the molecule detaching from one electrode) is evidenced by a sudden drop of I_{CON} to I_{DIS}. The data from the I(t) readouts is clustered by our stepfinder, without any pre-selection, providing the dwell-times (τ) for all the connection and disconnection events τ_{CON} and τ_{DIS}, respectively. The current corresponding to a trapped molecule (I_M) is extracted by the difference between I_{CON} and I_{DIS} ($I_M = I_{CON} - I_{DIS}$). The single-molecule junction conductance, G, is calculated according to $G = I_M/V_{bias}$. V_{bias} is set to 3 mV in all experiments close. The chronology of the selected laser power densities in the single-molecule experiments is random.

To date, multiple optically induced atomic rearrangements of the Au electrodes have been reported due to the presence of a tightly focused laser beam and enhanced fields, which increase the light absorption and thereby the thermal effects. They can be photon-assisted formed picocavities[6,7] and the thermal atomic expansion of the electrodes.[8] The later is the most relevant for PBJ measurments since it results in variation of the nanogap on the sub-angstrom scale able to switch atomic-sized metalic contacts,[9,10] and to restructure the STM tip electrodes.[11–13] To avoid the mentioned optically promoted atomic rearrangement of the Au nanogap, in the experimental routine employed, prior to the single-molecule measurements, the laser is switched-ON and focused on the interelectrode nanogap with the current-feedback loop of the STM activated. In this way, the nanogap is precisely adapted to the size of the benzenedithiol molecule and any induced angstrom sized[10] variation of the nanogap can be corrected. Once the nanogap has stabilised under laser illumination, after a resting time of ca. 1 hour, since the timescales of heat diffusion along the tip axis are shorter, single molecule detection experiments can be started with all possible optically promoted modifications on the electrodes already present.[12,13] In addition, in order not to optically alter the electrodes during the measurements, the laser power is maintained for the whole duration of the experiment and the irradiation is applied uninterruptedly (without beam chopping). The laser is switched-OFF after the experiments.

1.3 Chemicals, glassware, and sample preparation

All glassware and homemade PTFE/glass cells are cleaned with freshly prepared Piranha solution (volume ratio of 3:1 H_2SO_4:H_2O_2) before the experiments and subsequently rinsed with 18.2 Mω·cm^{-1} Milli-Q water (Millipore). A Au(111) single crystal (10 mm x 4 mm, MaTecK) of 5N purity, orientation accuracy of $< 0.1^\circ$ and roughness < 0.01 micron is employed as a substrate. Before each experiment, the Au(111) is cleaned with Piranha solution to eliminate possible residual contamination, rinsed with Milli-Q water, annealed in a butane flame for 10 minutes and then cooled down in Ar (99.9999 %, Westfalen) atmosphere. The crystal is then immediately immersed in an Ar-purged 0.01 mM ethanolic BDT solution for 5 h (submonolayer concentration).[1] The functionalised Au (111) substrate electrode's surface with DBT is washed thoroughly with ethanol and Milli-Q water, dried under a stream of Ar and the electrode is assembled in the STM cell. A volume of 80 µL of MilliQ water is added to the cell, to protect the surface against contamination.[14] MilliQ water is used as the working medium because of its purity, low conductivity and excellent heat dissipation.[15–17] The tip electrodes are cut from a 0.25 mm diameter Au wire (Alfa Aesar, Premion, 99.9985% metal basis) to be of ca. 1.5 cm length and electrochemically etched.[18] The etching procedure

provides plasmonic-active tips with homogeneous, sharp, symmetrical pencil-shaped apexes of ca. 50 nm diameter. After etching, the tips are coated three consecutive times with Zapon lack (CLOU, Germany) and dried overnight in Ar atmosphere to minimize leakage current when immersed in the working liquid. The leakage current of our tips is typically <10 pA.

2 Laser power density and nearfield gradient calculations

The laser power densities have been calculated assuming the far-field focus radius in the diffraction-limited of 316.4 nm (λ/2, with λ= 632.8 nm), or a far-field area of 7.86×10^{-2} mW/μm^2. The laser power was measured in air conditions in the far-field focus. Note that the estimated power density values represent an upper limit due to aberrations. In-air to in-water losses due to aberrations have previously been estimated for our setup to reach a factor 3 to 5.[2]

The nearfield gradients in the interelectrode nanogap are estimated by converting the power density (P) into a farfield strength (E) according to $P = E^2/Z_0$,[19] where Z_0 is the characteristic impedance of free space, and by assuming a field intensity enhancement of ca. 1000 for our setup.[2] The field gradient at 0 mW laser power is calculated employing the applied bias voltage of 3 mV and the interelectrode distance of 1 nm according to the 1,4-benzenedithiol's (BDT) bridge contact geometry.[4,5] k_BT/nm has been estimated assuming a gap temperature of 308.15 K (T based on the estimated local temperature increase of 10 K with respect to room temperature for setups with field enhancements in the order of 20 to 30 comparable to ours[17]).

Table S. 1 Calculated laser power density and field gradients values, for the different farfield laser powers employed in this work.

Laser power (mW)	Laser power density (mW/μm^2)	Field gradient (V/m)	k_BT/nm
0.0	0.0	3.0×10^6 (due to the applied voltage bias of 3 mV)	1.2×10^{-1}
3.8×10^{-1}	1.2	2.1×10^7	8.0×10^{-1}
1.3	4.1	4.0×10^7	1.4
1.9	6.0	4.8×10^7	1.7
2.8	8.9	5.8×10^7	2.1
3.3	1.1×10^1	6.3×10^7	2.2

3 Stepfinder based on hidden Markov model

3.1 Description

We have developed an automatised states finder, written in Python and based on the hidden Markov model (HMM) formalism,[20] to classify (cluster) the current levels in an unbiased way and hence excluding any manual data inspection.[21,22] The HMM formalism, based on stochastic Markov processes,[23] is a probabilistic or statistical model for inferring unobserved (hidden) information from observed data.[21,24] It describes the joint probability of a system based on a set of discrete observed and hidden variables or states (i.e., the Markov processes).

Our tool is an unsupervised (machine) learning framework for time series analysis that relies, as it is common in HMM methodologies, on three cornerstones based on specific tools as it follows.[24] (i) The evaluation of the sequences' likelihood (probability of a state at a specific time step).[25] (ii) the decoding procedure that finds the optimal hidden states' sequence that yields to the observed sequence in the I(t) readouts. (iii) the training of the HMM to best fit the observed data and the expected hidden state(s). The decoding has been based on the Viterbi decoding algorithm[26] and the training (learning) on the Baum-Welch,[20,21] both of them recursive procedures. The latter is a special case of expectation–maximization iterative algorithm aimed to find the unknown parameters of HMMs, to learn the model. Thanks to combine the three cornerstones we can identify and to cluster the different current levels, linked to distinctive connection and disconnection states, present in the I(t) readouts. Accordingly, the total τ_{CON} and τ_{DIS} can be extracted by classifying the datapoints of the whole I(t) readout datasets, for each laser power density (Figure S.1). Our HMM-based methodology demonstrated efficient clustering, as attested by the confusion matrix (Figure S.2) which summarises the comparison between automatic classification and manual inspection of 50 I(t) readout samples of 5 seconds each, with randomly selected laser power densities.

3.2 Example of classification HMM-based clustering methodology

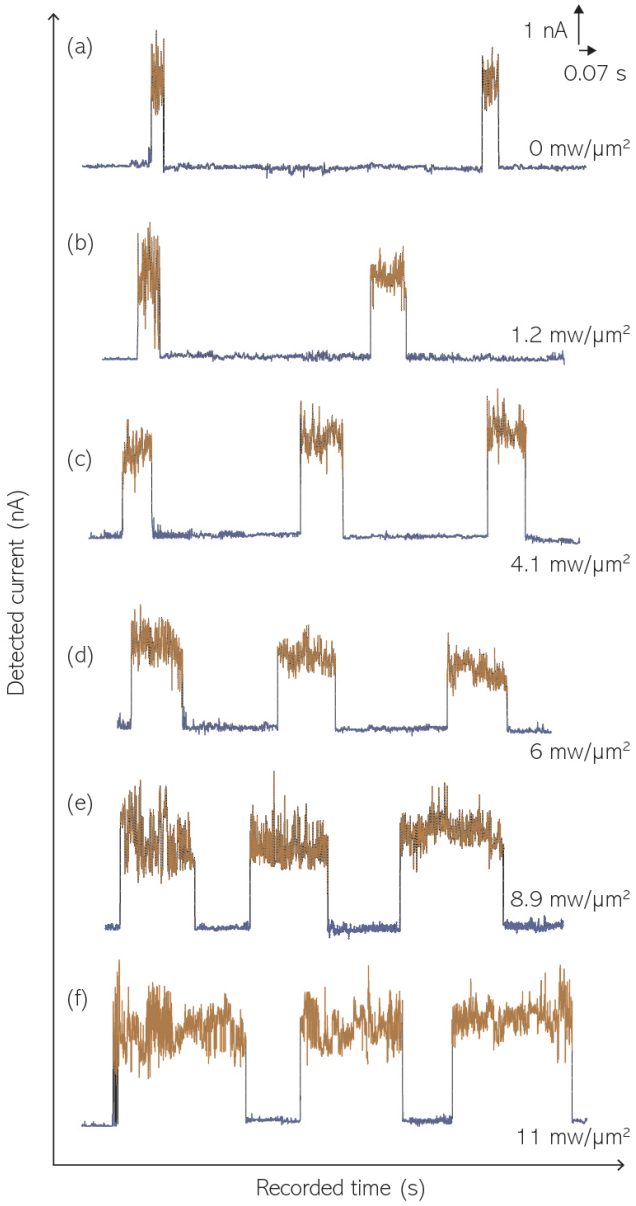

Fig S. 1 Example of data clustering I(t) readout (black), with classified connection (orange) and disconnection (blue) events for the different laser power densities indicated in the figure.

3.3 Evaluation of the HMM-based clustering methodology

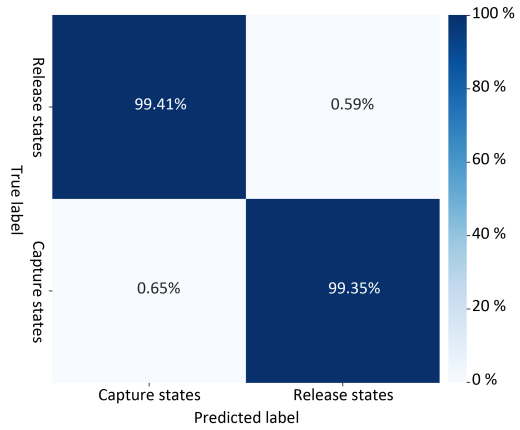

Fig S. 2 Evaluation results for the clustering accuracy of our HMM-based clustering methodology. The confusion matrix was built by 50 samples of 5 seconds of randomly selected laser power densities comparing the classification obtained by manual (true label) data inspection and feeding our clustering methodology (clustered label). The accuracy percentage in each confusion matrix panel represent the numbers of states clustered by the process with respect the the (true) manual classification. The diagonal (1, 1)th and (2, 2)th terms of the matrix indicate the discrimination accuracy of the clustering.

References

1 A. C. Aragonès and K. F. Domke, *Cell Reports Physical Science*, 2021, 2, 100389.

2 N. Martín Sabanés, L. M. A. Driessen and K. F. Domke, *Analytical Chemistry*, 2016, 88, 7108–7114.

3 J. D. Hunter, *Computing in Science Engineering*, 2007, 9, 90–95.

4 S. Kaneko, D. Murai, S. Marqués-González, H. Nakamura, Y. Komoto, S. Fujii, T. Nishino, K. Ikeda, K. Tsukagoshi and M. Kiguchi, *Journal of the American Chemical Society*, 2016, 138, 1294–1300.

5 S. Kaneko, E. Montes, S. Suzuki, S. Fujii, T. Nishino, K. Tsukagoshi, K. Ikeda, H. Kano, H. Nakamura, H. Vázquez and M. Kiguchi, *Chemical Science*, 2019, 10, 6261–6269.

6 F. Benz, M. K. Schmidt, A. Dreismann, R. Chikkaraddy, Y. Zhang, A. Demetriadou, C. Carnegie, H. Ohadi, B. De Nijs, R. Esteban, J. Aizpurua and J. J. Baumberg, *Science*, 2016.

7 C. Carnegie, J. Griffiths, B. De Nijs, C. Readman, R. Chikkaraddy, W. M. Deacon, Y. Zhang, I. Szabó, E. Rosta, J. Aizpurua and J. J. Baumberg, *Journal of Physical Chemistry Letters*, 2018.

8 D. Guhr, D. Rettinger, J. Boneberg, A. Erbe, P. Leiderer and E. Scheer, *Journal of Microscopy*, 2008, 229, 407–414.

9 W. Zhang, H. Liu, J. Lu, L. Ni, H. Liu, Q. Li, M. Qiu, B. Xu, T. Lee, Z. Zhao, X. Wang, M. Wang, T. Wang, A. Offenhäusser, D. Mayer, W.-T. Hwang and D. Xiang, *Light: Science & Applications*, 2019, 8, 34.

10 S. Zhang, C. Guo, L. Ni, K. M. Hans, W. Zhang, S. Peng, Z. Zhao, D. C. Guhr, Z. Qi, H. Liu, M. Song, Q. Wang, J. Boneberg, X. Guo, T. Lee, E. Scheer and D. Xiang, *Nano Today*, 2021, 39, 101226.

11 J. Jersch and K. Dickmann, *Applied Physics Letters*, 1996, 68, 868–870.

12 J. Boneberg, H.-J. Münzer, M. Tresp, M. Ochmann and P. Leiderer, *Applied Physics A*, 1998, 67, 381–384.

13 R. Huber, M. Koch and J. Feldmann, *Applied Physics Letters*, 1998, 73, 2521–2523.

14 A. Aragonès, A. C. Aragonès, N. L. Haworth, S. Ciampi, N. J. Bloomfield, G. G. Wallace, M. L. Coote, I. Diez-Perez and N. Darwish, *Protocol Exchange*, 2016.

15 W. Zhang, T. Schmid, B.-S. Yeo and R. Zenobi, *The Journal of Physical Chemistry C*, 2008, 112, 2104–2108.

16 A. V. Malkovskiy, V. I. Malkovsky, A. M. Kisliuk, C. A. Barrios, M. D. Foster and A. P. Sokolov, *Journal of Raman Spectroscopy*, 2009, 40, 1349–1354.

17 J. Rigor, D. Kurouski and N. Large, *The Journal of Physical Chemistry C*, 2022, 126, 13986–13993.

18 B. Ren, G. Picardi and B. Pettinger, *Review of Scientific Instruments*, 2004, 75, 837–841.

19 C. Balanis, *John Wiley & Sons, Inc.*, 2016.

20 L. E. Baum, T. Petrie, G. Soules and N. Weiss, *The Annals of Mathematical Statistics*, 1970, 41, 164–171.

21 J. Bilmes, *A Gentle Tutorial of the EM algorithm and its application to Parameter Estimation for Gaussian Mixture and Hidden Markov Models*, ICSI Technical Report TR-97-021, 1997.

22 E. Coviello, A. B. Chan and G. R. G. Lanckriet, *Journal of Machine Learning Research*, 2014, 15, 697–747.

23 A. A. Markov, 1975, 42, 3–375.

24 L. Rabiner, *Proceedings of the IEEE*, 1989, 77, 257–286.

25 A. P. Dempster, N. M. Laird and D. B. Rubin, *Journal of the Royal Statistical Society. Series B (Methodological)*, 1977, 39, 1–38.

26 A. Viterbi, *IEEE Transactions on Information Theory*, 1967, 13, 260–269.